

# Explaining DAMA with proton–philic spin–dependent inelastic Dark Matter (pSIDM): a frequentist analysis

Seong–Hyeong Kang Stefano Scopel Jong–Hyun Yoon

Department of Physics, Sogang University, Seoul, South Korea

E-mail: [scopel@sogang.ac.kr](mailto:scopel@sogang.ac.kr), [francis735@naver.com](mailto:francis735@naver.com), [pledge200@gmail.com](mailto:pledge200@gmail.com)

**Abstract.** Proton–philic spin–dependent inelastic Dark Matter (pSIDM) is a Weakly Inelastic Massive Particle (WIMP) scenario that can explain the DAMA yearly modulation effect in compliance with the constraints from other direct detection Dark Matter (DM) searches. We obtain updated ranges for its parameters both in a halo–independent approach and adopting a truncated Maxwellian for the WIMP velocity distribution constructing approximate frequentist confidence intervals from an effective chi–square including, among others, the latest experimental constraints from XENON1T PANDAX–II, SuperCDMS and CDMSlite. In the halo–independent analysis we have implemented the dependence on the WIMP velocity distribution through a step–wise parameterization of the halo function. Since in the pSIDM the WIMP incoming velocities required to explain the DAMA effect fall in a narrow range close to the escape velocity a limited number of steps was sufficient to determine the profile likelihood of the parameters. For the calculation of the profile likelihood we used a Markov Chain Montecarlo (MCMC) generator that required a large number of evaluations of the expected rates. To reduce computational time we introduced expected rates expressions rearranged in terms of differences of singled–valued integrated response functions suitable for a fast evaluation through tabulation and interpolation. Our frequentist analysis confirms the present viability of the pSIDM scenario as a possible explanation of the DAMA effect. In terms of the WIMP mass  $m_\chi$  and of the mass splitting  $\delta$  we find the 1–sigma ranges  $12.5 \text{ GeV} \leq m_\chi \leq 15.7 \text{ GeV}$ ,  $22.1 \text{ keV} \leq \delta \leq 26.1 \text{ keV}$  for the halo–independent analysis and  $11.4 \text{ GeV} \leq m_\chi \leq 13.6 \text{ GeV}$ ,  $24.4 \text{ keV} \leq \delta \leq 27.0 \text{ keV}$  for the Maxwellian case. We find that a full year of data taking of XENON1T should allow to start probing the pSIDM scenario.

---

## Contents

<b>1</b>	<b>Introduction</b>	<b>1</b>
<b>2</b>	<b>The pSIDM scenario and DAMA</b>	<b>2</b>
<b>3</b>	<b>Expected rates and response functions</b>	<b>3</b>
<b>4</b>	<b>Results</b>	<b>10</b>
4.1	The halo-independent case	11
4.2	The Maxwellian case	13
<b>5</b>	<b>Conclusions</b>	<b>15</b>
<b>A</b>	<b>Experimental constraints</b>	<b>17</b>
A.1	DAMA	17
A.2	XENON1T and PANDAX-II	17
A.3	PICO-2L, COUPP and PICASSO	18
A.4	SuperCDMS and CDMSlite	19

---

## 1 Introduction

A worldwide experimental effort is under way to detect Weakly Interacting Massive Particles (WIMPs), which are considered the most natural candidates to provide the Dark Matter (DM) in the halo of our Galaxy, and the direct search for their recoils off nuclear targets represents the most direct way to detect them [1–7]. For quite a long time this search has been driven by theory, and tailored on the search of the Supersymmetric neutralino, or on other specific DM candidates provided by ultraviolet theoretical completions of the Standard Model, believed to be observable in accelerator physics. However the non-observation so far of new physics at the Large Hadron Collider (LHC) has strongly prompted for the necessity to go beyond this ”to-down” approach in order to extend the search of Dark Matter candidates to a wider range of properties through an alternative ”bottom-up” strategy not biased by theoretical prejudice. Such a *model-independent* approach to WIMP direct searches must address two issues: how to compare results from experiments using different targets (i.e. which scaling law to adopt for the WIMP–nucleus cross section) and which velocity distribution determines the WIMP flux on Earth. Both these issues have been addressed in the last few years: in particular, the WIMP–nucleus cross section can be parameterized in terms of the most general non-relativistic effective theory complying with Galilean symmetry [8, 9] including modifications of the scattering kinematics due to a possible inelasticity of the scattering process [10], while a halo-independent way to compare the results of different experiments has been introduced by factorizing the dependence of expected rates on the WIMP velocity distribution  $f(v)$  in a single halo function  $\eta(v)$ [11]. In particular, maximum-likelihood methods have been applied to determine  $\eta$  and the particle physics parameters, as well as statistical methods to assess the compatibility of different experimental results [12–18]. In such analyses a likelihood function is introduced in terms of a step-wise parameterization of the  $\eta$  function (or, alternatively,  $f(v)$  is expressed in terms of a sum of  $\delta$  functions) that,

under some conditions, is proved to maximize the likelihood for a fixed number of steps. However, while it is in principle straightforward to find in this way the DM parameters that maximize the profile likelihood function treating  $\eta$  as a set of nuisance parameters, as long as the presence of a DM signal in the existing data is not established the result has little meaning since one would always obtain a best-fit point even for highly incompatible data sets.

In the present paper we wish to apply such likelihood methods to a specific WIMP scenario, where, instead, a very strong DM signal has been established in the data and that has already been shown to allow a full compatibility among different experiments: proton–philic spin-dependent inelastic Dark Matter (pSIDM). Specifically, such scenario was introduced in [19] to explain the DAMA yearly modulation effect [1] in compliance with existing constraints, and is summarized in Section 2. In particular, in the following we will use for the pSIDM a likelihood function for which the theorems mentioned above on the number of steps do not hold. However in the pSIDM the WIMP incoming velocities required to explain DAMA fall in a narrow range close to the escape velocity so that, in practice, a limited number of steps in the  $\eta$  parameterization will indeed be enough (this will be confirmed by numerical inspection). In this way we will get updated ranges for the pSIDM parameters  $m_\chi$  (WIMP mass),  $\delta$  (mass splitting) and  $r = c^n/c^p$  (neutron-to-proton coupling ratio) by constructing approximate frequentist confidence intervals from an effective chi-square including, among others, the latest experimental constraints from XENON1T [2], PANDAX-II [3], SuperCDMS [4] and CDMSlite [5]. Our analysis will confirm the present viability of the pSIDM scenario as a possible explanation of the DAMA effect. We will also integrate such halo-independent result with a more standard analysis with the velocity distributions  $f(v)$  given by a truncated Maxwellian.

For the calculation of the profile likelihood of the pSIDM parameters we will use emcee [20], a Markov Chain Montecarlo (MCMC) generator. The numerical procedure is straightforward but requires a large number of evaluations of the expected rates for DAMA and the other experiments included in the analysis (listed in Appendix A). This would be time consuming if the relevant experimental response functions were calculated at run time. For this reason in Section 3 we provide expected rates expressions rearranged in terms of differences of singled-valued functions that can be tabulated and interpolated.

## 2 The pSIDM scenario and DAMA

In this Section we briefly summarize the features of the scenario introduced in Ref. [19] (we refer the reader to such paper for further details).

The most stringent bounds on an interpretation of the DAMA effect in terms of WIMP–nuclei scatterings are obtained by detectors using xenon (LUX [2, 21–23], PANDA [3, 24, 25]) and germanium (CDMS [4, 5, 26–29]) whose spin is mostly originated by an unpaired neutron, as well as by the KIMS experiment [30–32] which uses  $CsI$  and thus directly probes the contribution to the DAMA effect from WIMP scatterings off iodine targets. If the WIMP mass is small enough to assume that the DAMA signal is only due to WIMP scatterings off sodium the KIMS constraint can be evaded. Moreover, both sodium and iodine in DAMA have an unpaired proton, so that if the WIMP particle interacts with ordinary matter predominantly via a spin-dependent coupling which is suppressed for neutrons it can explain the DAMA effect in compliance with the bounds from xenon and germanium detectors, whose constraints are strongly relaxed [33, 34]. However this scenario is constrained by droplet detec-

tors (SIMPLE[35], COUPP[7]) and bubble chambers (PICASSO[36], PICO-2L[6, 37], PICO-60[38]) which all use nuclear targets with an unpaired proton (in particular, they all contain  $^{19}\text{F}$ , while SIMPLE contains also  $^{35}\text{Cl}$  and  $^{37}\text{Cl}$  and COUPP and PICO-60 use also  $^{127}\text{I}$ ). As a consequence, this class of experiments rules out a DAMA explanation in terms of WIMP elastic scatterings with a spin-dependent coupling to protons when standard assumptions are made on the WIMP local density and velocity distribution in our Galaxy[34, 37].

In Ref.[19] the alternative approach of Inelastic Dark Matter (IDM) was proposed to reconcile DAMA to fluorine detectors. In this class of models a DM particle  $\chi_1$  of mass  $m_{\chi_1} = m_\chi$  interacts with atomic nuclei exclusively by up-scattering to a second heavier state  $\chi_2$  with mass  $m_{\chi_2} = m_\chi + \delta$ . A peculiar feature of IDM is that there is a minimal WIMP incoming speed in the lab frame matching the kinematic threshold for inelastic upscatters and given by:

$$v_{min}^* = \sqrt{\frac{2\delta}{\mu_{\chi N}}}, \quad (2.1)$$

with  $\mu_{\chi N}$  the WIMP-nucleus reduced mass. This quantity corresponds to the lower bound of the minimal velocity  $v_{min}$  (also defined in the lab frame) required to deposit a given recoil energy  $E_R$  in the detector:

$$v_{min} = \frac{1}{\sqrt{2m_N E_R}} \left| \frac{m_N E_R}{\mu_{\chi N}} + \delta \right|, \quad (2.2)$$

with  $m_N$  the nuclear mass. In particular, indicating with  $v_{min}^{*Na}$  and  $v_{min}^{*F}$  the values of  $v_{min}^*$  for sodium and fluorine, and with  $v_{cut}$  the result of the boost in the lab rest frame of some maximal speed value beyond which the WIMP velocity distribution  $f(v)$  in the galactic rest frame vanishes (typically  $v_{cut}$  is identified with the WIMP escape velocity  $v_{esc}$ ), constraints from droplet detectors and bubble chambers can be evaded when the WIMP mass  $m_\chi$  and the mass gap  $\delta$  are chosen in such a way that the hierarchy:

$$v_{min}^{*Na} < v_{cut}^{lab} < v_{min}^{*F}, \quad (2.3)$$

is achieved, since in such case WIMP scatterings off fluorine turn kinematically impossible while those off sodium can still serve as an explanation to the DAMA effect. Clearly, this mechanism rests on the trivial observation that the velocity  $v_{min}^*$  for fluorine is larger than that for sodium.

As a consequence of what discussed above, in the pSIDM scenario the WIMP-nucleus interaction must be fixed to a spin-dependent coupling, which in the most simple case corresponds to

$$\mathcal{L}_{int} \ni c^p \vec{S}_\chi \cdot \vec{S}_p + c^n \vec{S}_\chi \cdot \vec{S}_n, \quad (2.4)$$

with  $\mathcal{N} = p, n$ , while the parameter  $r = c^n/c^p \ll 1$  will be allowed to vary freely and its range will be determined by the likelihood analysis of Section 4.

### 3 Expected rates and response functions

The expected rate in a given visible energy bin  $E'_1 \leq E' \leq E'_2$  of a direct detection experiment is given by:

$$R_{[E'_1, E'_2]} = MT \int_{E'_1}^{E'_2} \frac{dR}{dE'} dE' \quad (3.1)$$

$$\frac{dR}{dE'} = \sum_T \int_0^\infty \frac{dR_{\chi T}}{dE_{ee}} \mathcal{G}_T(E', E_{ee}) \epsilon(E') dE_{ee} \quad (3.2)$$

$$E_{ee} = q(E_R) E_R, \quad (3.3)$$

with  $\epsilon(E') \leq 1$  the experimental efficiency/acceptance. In the equations above  $E_R$  is the recoil energy deposited in the scattering process (indicated in keVnr), while  $E_{ee}$  (indicated in keVee) is the fraction of  $E_R$  that goes into the experimentally detected process (ionization, scintillation, heat) and  $q(E_R)$  is the quenching factor,  $\mathcal{G}_T(E', E_{ee} = q(E_R) E_R)$  is the probability that the visible energy  $E'$  is detected when a WIMP has scattered off an isotope T in the detector target with recoil energy  $E_R$ ,  $M$  is the fiducial mass of the detector and  $T$  the live-time of the data taking. Moreover,

$$\frac{dR_{\chi T}}{dE_R} = N_T \int_{v_{min}}^{v_{esc}} \frac{\rho_\chi}{m_\chi} v \frac{d\sigma_{\chi T}}{dE_R} f(v) dv, \quad (3.4)$$

where  $N_T$  is the number of targets T per unit mass, while  $\rho_\chi$  and  $m_\chi$  are the WIMP local density and mass. The most general WIMP–nucleon interaction [39] (including momentum and velocity dependence) can be parameterized by making use of the interaction Hamiltonian which descends from non-relativistic EFT[8, 9]:

$$\mathcal{H} = \sum_{\tau=0,1} \sum_{k=1}^{15} c_k^\tau \mathcal{O}_k t^\tau, \quad (3.5)$$

where  $t^0 = 1$ ,  $t^1 = \tau_3$  denote the  $2 \times 2$  identity and third Pauli matrix in isospin space, respectively, the dimensional -2 isoscalar and isovector coupling constants  $c_k^0$  and  $c_k^1$  are related to those to protons and neutrons  $c_k^p$  and  $c_k^n$  by  $c_k^p = (c_k^0 + c_k^1)/2$  and  $c_k^n = (c_k^0 - c_k^1)/2$  and the operators  $\mathcal{O}_i$  are for instance listed in Equations (12) and (13) of [9]. Using the notation of [9]:

$$\frac{d\sigma_{\chi T}}{dE_R} = \frac{1}{10^6} \frac{2m_T}{4\pi} \frac{c^2}{v^2} \left[ \frac{1}{2j_\chi + 1} \frac{1}{2j_T + 1} \sum_{spin} |\mathcal{M}_T|^2 \right], \quad (3.6)$$

with:

$$\frac{1}{2j_\chi + 1} \frac{1}{2j_T + 1} \sum_{spin} |\mathcal{M}_T|^2 = \frac{4\pi}{2j_T + 1} \sum_{\tau\tau'} \sum_l R_l^{\tau\tau'} W_{T,l}^{\tau\tau'}, \quad (3.7)$$

and, including velocity-dependent terms:

$$R_l^{\tau\tau'} = R_{0,l}^{\tau\tau'} + R_{1,l}^{\tau\tau'} (v^2 - v_{min}^2). \quad (3.8)$$

The factor  $10^{-6}$  in front of Eq. (3.6) is to express the differential cross section in  $\text{GeV}^{-2}/\text{keV}$  if the  $c_k^\tau$  couplings are expressed in  $\text{GeV}^{-2}$ . The WIMP response functions  $R_l^{\tau\tau'}$  are provided in Eq.(38) of [9] (but in the equation above the factor  $q^2/m_n^2$  that multiplies

the last 5 terms in Eq. (40) of [9] have been incorporated in the definitions of the  $R_l^{\tau\tau'}$ 's) and  $l=M, \Sigma'', \Sigma', \Phi'', \Phi''M, \tilde{\Phi}', \Delta, \Delta\Sigma'$  represent one of the possible nuclear interaction types. As far as the pSIDM scenario is concerned, it can be implemented with any interaction operator with an exclusively spin-dependent nuclear response function (i.e. depending only on either the function  $W_{\Sigma''}^{\tau\tau'}$  or  $W_{\Sigma'''}^{\tau\tau'}$  in the notation of [19]). Such operators, for instance summarized in Table 2 of Ref. [39], correspond to  $k=4, 6, 7, 9, 10$  and  $14$ . In particular, in the present analysis we only consider the standard spin dependent case, which in Eq.(3.5) and the notation of ([8, 9]) corresponds to  $k=4$ . In the case of a single coupling we factorize the *conventional* WIMP-proton cross section:

$$\sigma_p = (c_4^p)^2 \frac{\mu_{\chi N}^2}{\pi}, \quad (3.9)$$

with  $\mu_{\chi N}$  the WIMP-nucleon reduced mass<sup>1</sup>. Combining everything together and inverting the order of the two integrals in  $E_R$  and  $v$ [40], for inelastic scattering one gets:

$$\int_0^\infty dE_R \int_{v_{min}}^\infty dv \rightarrow \int_{v_{min}^*}^\infty dv \int_{E_R^-(v)}^{E_R^+(v)} dE_R, \quad (3.10)$$

where the quantities  $E_R^\pm(v, m_\chi, \delta)$  represent the two values of  $E_R$  which correspond to the same  $v_{min}$ , i.e.:

$$E_R^\pm(v_{min}, m_\chi, \delta) = \frac{\mu_{\chi N}^2}{m_N} \left[ v_{min}^2 - \frac{(v_{min}^*)^2}{2} \pm \sqrt{v_{min}^2 - (v_{min}^*)^2} \right], \quad (3.11)$$

(a schematic view of the mapping between  $E_R$  and  $v_{min}$  for inelastic scattering is illustrated in Fig.1). Then:

$$R_{[E'_1, E'_2]} = \frac{\rho_\chi}{m_\chi} \sigma_p \int_{v_{min}^*}^\infty dv \hat{\mathcal{H}}(v) f(v), \quad (3.12)$$

with:

$$\begin{aligned} \hat{\mathcal{H}}(v) = & \sum_T N_T M T \frac{c^2}{v} \frac{m_T}{\mu_{\chi T}^2} \frac{2\pi}{10^6} \int_{E_R^-(v)}^{E_R^+(v)} dE_R \int_{E'_1}^{E'_2} dE' \epsilon(E') \mathcal{G}_T[E', q(E_R) E_R] \times \\ & \frac{1}{2j_T + 1} \sum_{\tau\tau'} \sum_l \left[ \hat{R}_{0,l}^{\tau\tau'} + \hat{R}_{1,l}^{\tau\tau'} (v^2 - v_{min}^2) \right] W_l^{\tau\tau'} = \end{aligned} \quad (3.13)$$

$$\frac{c^2}{v} \int_{E_R^-(v)}^{E_R^+(v)} dE_R \left\{ \hat{\mathcal{R}}_0(E_R) + \hat{\mathcal{R}}_1(E_R) (v^2 - v_{min}(E_R)^2) \right\}, \quad (3.14)$$

and:

$$\begin{aligned} \hat{\mathcal{R}}_{\{0,1\}} = & \sum_T N_T M T \frac{m_T}{\mu_{\chi T}^2} \frac{2\pi}{10^6} \int_{E'_1}^{E'_2} dE' \epsilon(E') \mathcal{G}_T[E', q(E_R) E_R] \frac{1}{2j_T + 1} \sum_{\tau\tau'} \sum_l \hat{R}_{\{0,1\},l}^{\tau\tau'} W_l^{\tau\tau'} \\ = & \sum_T \left[ \hat{\mathcal{R}}_{\{0,1\}} \right]_T, \end{aligned} \quad (3.15)$$

---

<sup>1</sup>The standard WIMP-proton cross section corresponds to  $3/16 \sigma_p$ .

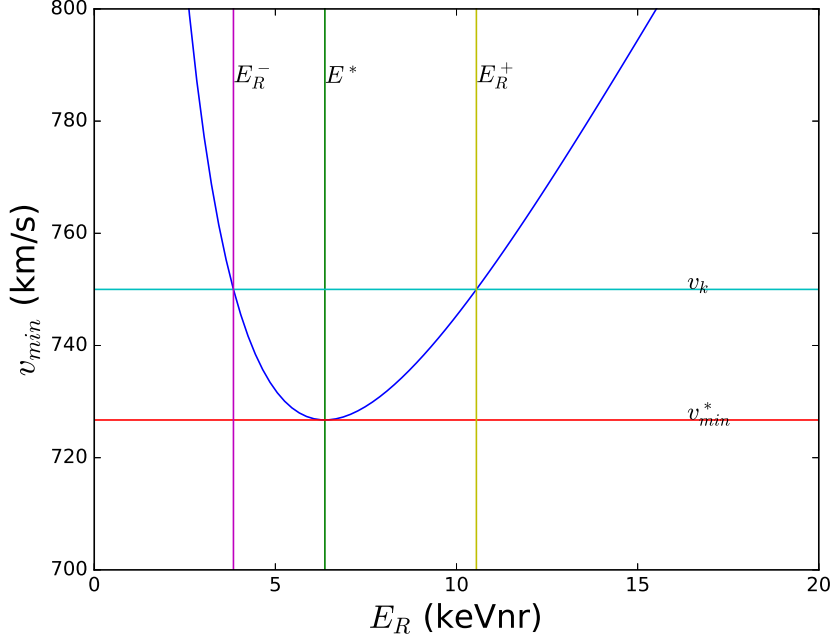


**Figure 1.** Mapping between  $E_R$  and  $v_{min}$  in  $^{23}\text{Na}$  for  $m_\chi=10$  GeV and  $\delta=20$  keV.

where  $\hat{R}_{0,l}^{\tau\tau'} \equiv R_{0,l}^{\tau\tau'}/(c_4^p)^2$ . Setting[40]:

$$f(v) \equiv -v \frac{d}{dv} \eta(v), \quad (3.16)$$

and integrating by parts one gets:

$$R_{[E'_1, E'_2]} = \frac{\rho_\chi}{m_\chi} \sigma_p \int_0^\infty dv \hat{\mathcal{R}}(v) \eta(v) = \int_0^\infty dv \mathcal{R}(v) \tilde{\eta}(v), \quad (3.17)$$

with:

$$\tilde{\eta}(v, t) = \frac{\rho_\chi}{m_\chi} \sigma \eta(v, t), \quad \eta(v, t) = \int_v^\infty \frac{f(v, t)}{v} dv, \quad (3.18)$$

and where now the response function  $\hat{\mathcal{R}}$  depends on  $\hat{\mathcal{H}}$  through:

$$\hat{\mathcal{R}}(v) = \frac{d}{dv} \left[ v \hat{\mathcal{H}}(v) \right]. \quad (3.19)$$

In Eq.(3.18) we have explicitly indicated that the the generalized halo function  $\tilde{\eta}$  depends, as the velocity distribution  $f(v)$ , on time  $t$ , due to the rotation of the Earth around the Sun. In particular, the generalized halo function  $\tilde{\eta}(v)$  is common to all experiments, while the response function  $\mathcal{R}(v)$  depends on experimental inputs. Notice that in Eq.(3.18) all quantities depend on  $v = |\vec{v}|$  because present experiments have no directional sensitivity, so  $\mathcal{R}(\vec{v}) = \mathcal{R}(v)$ . This means that in (3.18) one has  $\tilde{\eta}(v) \equiv \int d\Omega v^2 \tilde{\eta}(\vec{v})$  and  $f(v) \equiv \int d\Omega v^2 f(\vec{v})$ , i.e. present experiments are not sensitive to the angular dependence of the velocity distribution if the

latter is expressed in the detector's reference frame. Due to this latter property, that ensures the validity of Eq.(3.17) for any velocity distribution, in the following we choose to express the rate in the lab rest frame.

Given a time-dependent signal  $S(t) \equiv R_{[E'_1, E'_2]}(t)$ , present direct detection experiments have either access to the time average of  $S$ , i.e.:

$$\begin{aligned} S_0 &\equiv \frac{1}{T} \int_0^T S(t) dt = \int_0^\infty \mathcal{R}(v) \tilde{\eta}_0(v) dv, \\ \tilde{\eta}_0(v) &\equiv \frac{1}{T} \int_0^T \tilde{\eta}(v, t) dt, \end{aligned} \quad (3.20)$$

or, as in the case of the DAMA experiment, to the yearly modulation amplitude  $S_1$ , defined as the cosine transform of  $S$ :

$$\begin{aligned} S_1 &\equiv \frac{2}{T} \int_0^T \cos \left[ \frac{2\pi}{T} (t - t_0) \right] S(t) dt = \int_0^\infty \mathcal{R}(v) \tilde{\eta}_1(v) dv, \\ \tilde{\eta}_1(v) &\equiv \frac{2}{T} \int_0^T \cos \left[ \frac{2\pi}{T} (t - t_0) \right] \tilde{\eta}(v, t) dt, \end{aligned} \quad (3.21)$$

with  $T=1$  year and  $t_0=2$  June. In the halo independent method no assumptions are made on the velocity distribution  $f$ , so that the two halo functions  $\tilde{\eta}_0(v)$  and  $\tilde{\eta}_1(v)$  are subject to the very general conditions:

$$\begin{aligned} \tilde{\eta}_0(v_2) &\leq \tilde{\eta}_0(v_1) \quad \text{if } v_2 > v_1, \\ |\tilde{\eta}_1| &\leq \tilde{\eta}_0 \quad \text{at the same } v, \\ \tilde{\eta}_0(v \geq v_{esc}) &= 0, \end{aligned} \quad (3.22)$$

with  $v_{esc}$  the galactic escape velocity expressed in the lab rest frame. In particular, it has been recently shown that, for a given set of annual modulation experimental data, if the effect is totally ascribed to the time-dependent change of reference frame between the lab and the Galaxy, even in a halo-independent approach it is possible to improve the second constraint of Eq.(3.22), i.e. to get  $|\tilde{\eta}_1/\tilde{\eta}_0| < a$  with  $a < 1$  (namely, until now only an analysis of the DAMA data restricted to velocity distributions which are isotropic in the galactic rest frame is available, with values of  $a$  varying from  $\simeq 0.14$  and  $\simeq 0.25$  depending on the WIMP mass [41], although the same procedure can in principle be applied to the non-isotropic case). However, allowing for a possible variation of the WIMP local density  $\rho$  with the Earth's position, the general range of  $\tilde{\eta}_1$  given in Eq.(3.22) is in principle always saturated.

The continuous halo function  $\tilde{\eta}(v)$  depends in principle on an infinite number of parameters. However, for practical purposes a possible approach to this problem is to parameterize  $\tilde{\eta}_0(v)$  with a step function sampled in a large-enough number of velocity steps, i.e., to set:

$$\tilde{\eta}_{0,1}(v) = \sum_{k=1}^N \tilde{\eta}_{0,1}^k \theta(v - v_{k-1}) \theta(v_k - v), \quad (3.23)$$

or, equivalently:



$$\begin{aligned}
\tilde{\eta}_{0,1}(v) &= \sum_{k=1}^N \delta\tilde{\eta}_{0,1}^k \theta(v_k - v), \\
\delta\tilde{\eta}_{0,1}^k &\equiv \tilde{\eta}_{0,1}^k - \tilde{\eta}_{0,1}^{k-1}, \\
\delta\tilde{\eta}_0^k &> 0
\end{aligned} \tag{3.24}$$

with the relations:

$$\tilde{\eta}_{0,1}^k(v_{min}) = \sum_{i=k}^N \delta\tilde{\eta}_{0,1}^i, \tag{3.25}$$

in a *large-enough* set of velocity steps (streams),  $v = [v_1, \dots, v_N]$ . Actually, a halo function of the form (3.25) corresponds to a velocity distribution given by  $f(v) = \sum_k^N \lambda_k \delta(v - v_k)$  that has been understood in the literature to extremize “generalized moments” of the form (3.17), i.e.  $S = \int_{v^*}^{\infty} \mathcal{H}(v) f(v, t) dv$  in terms of  $N_c + 1$  streams when  $N_c$  experimental constraints  $S_k$ ,  $k = 1 \dots N_c$  (plus the normalization of  $f(v)$ ), are provided[41]. This has been used in the literature to minimize the likelihood function  $\mathcal{L}(f, S_k)$ [12, 13, 42] in terms of  $N \leq N_c + 1$  streams. Notice, however, that the likelihood function in the analysis of Section 4 will depend on the two independent halo functions  $\tilde{\eta}_0$  and  $\tilde{\eta}_1$ , so that in our case the number of streams  $N$  needed to minimize  $\mathcal{L}$  is not related to the number of experimental constraints  $N_c$ . However, as it is evident from Eq.(2.3), the pSIDM scenario that we wish to analyze leads to a velocity range for the DAMA modulation effect  $v_{DAMA}^{min} < v < v_{DAMA}^{max}$  which is compressed to values close to  $v_{esc}$  (typically,  $v_{esc} - v_{DAMA}^{min} \leq 50$  km/sec) so in such a small range a relatively small value of  $N$  still allows a good sampling of the halo functions  $\tilde{\eta}_{0,1}$ . In fact, taking into account the first of the requirements of Eq.(3.22), the halo function  $\tilde{\eta}_0$  that minimizes the tension between DAMA and the constraints of other experiments (and so maximizes the likelihood function used in Section 4) is given by the minimal one that can explain the DAMA effect, i.e. to a halo function  $\tilde{\eta}_0$  monotonically decreasing with  $v_{min}$  that saturates the condition in the second line of Eq.(3.22) and flattens-out below  $v_{DAMA}^{min}$ , i.e.  $\tilde{\eta}(v < v_{DAMA}^{min}) = \tilde{\eta}(v_{DAMA}^{min})$ . The former condition implies:

$$\tilde{\eta}_{0,k} = \max_{i>k} |\tilde{\eta}_{1,i}|, \tag{3.26}$$

while the latter corresponds to:

$$\delta\tilde{\eta}_1^k = 0 \text{ for } v_k < v_{DAMA}^{min}. \tag{3.27}$$

As a consequence of the considerations above, in Section 4 we will adopt the  $\tilde{\eta}_{1,k}$ ’s as free parameters subject to (3.27) and use (3.26) for the  $\tilde{\eta}_{0,k}$ ’s.

When the piece-wise definition of the  $\eta$  function (3.23) is used in (3.19) one gets:

$$R_{[E'_1, E'_2]} = N_T MT \frac{\rho_\chi}{m_\chi} \sigma \int_{v_{min}^*}^{\infty} dv \frac{d}{dv} \left\{ v \frac{c^2}{v} \int_{E_R^-(v)}^{E_R^+(v)} dE_R \left\{ \hat{\mathcal{R}}_0(E_R) + \hat{\mathcal{R}}_1(E_R) [v^2 - v_{min}(E_R)^2] \right\} \right\} \\ \times \sum_{k=1}^N \delta \tilde{\eta}^k \theta(v_k - v) = N_T MT \frac{\rho_\chi}{m_\chi} \sigma c^2 \sum_{k=1}^N \delta \tilde{\eta}^k \times \quad (3.28)$$

$$\int_{E_R^-(v)}^{E_R^{max}(v_k)} dE_R \left\{ \hat{\mathcal{R}}_0(E_R) + \hat{\mathcal{R}}_1(E_R) [v_k^2 - v_{min}(E_R)^2] \right\}. \quad (3.29)$$

Expanding explicitly the square of  $v_{min}(E_R)$  and setting:

$$\begin{aligned} \bar{\mathcal{R}}_{0,1}(E_R) &\equiv \int_0^{E_R} dE'_R \hat{\mathcal{R}}_{0,1}(E'_R) \\ \bar{\mathcal{R}}_{1E}(E_R) &\equiv \int_0^{E_R} dE'_R E'_R \hat{\mathcal{R}}_1(E'_R) \\ \bar{\mathcal{R}}_{1E^{-1}}(E_R) &\equiv \int_0^{E_R} dE'_R \frac{1}{E'_R} \hat{\mathcal{R}}_1(E'_R), \end{aligned} \quad (3.30)$$

the predicted rate can then be written as:

$$\begin{aligned} R_{[E'_1, E'_2]} &= \frac{\rho_\chi}{m_\chi} \sigma c^2 \sum_{k=1}^N \delta \tilde{\eta}^k \times \\ &\left\{ \bar{\mathcal{R}}_0 [E_R^{max}(v_k)] - \bar{\mathcal{R}}_0 [E_R^{min}(v_k)] + (v_k^2 - \frac{\delta}{\mu_{\chi N}}) (\bar{\mathcal{R}}_1 [E_R^{max}(v_k)] - \bar{\mathcal{R}}_1 [E_R^{min}(v_k)]) \right. \\ &- \frac{m_T}{\mu_{\chi N}^2} (\bar{\mathcal{R}}_{1E} [E_R^{max}(v_k)] - \bar{\mathcal{R}}_{1E} [E_R^{min}(v_k)]) \\ &\left. - \frac{\delta^2}{m_T} (\bar{\mathcal{R}}_{1E^{-1}} [E_R^{max}(v_k)] - \bar{\mathcal{R}}_{1E^{-1}} [E_R^{min}(v_k)]) \right\}, \end{aligned} \quad (3.31)$$

with:

$$(\bar{\mathcal{R}}_{0,1}, \bar{\mathcal{R}}_{1E}, \bar{\mathcal{R}}_{1E^{-1}}) = N_T MT (\bar{\mathcal{R}}_{0,1}, \bar{\mathcal{R}}_{1E}, \bar{\mathcal{R}}_{1E^{-1}}). \quad (3.32)$$

The functions of Eq.(3.32) are quadratic in the two couplings  $c^n=c_4^n$  and  $c^p=c_4^p$  so that, in terms of  $r \equiv \frac{c^n}{c^p}$ :

$$\bar{\mathcal{R}}(r) = \frac{r(r+1)}{2} \bar{\mathcal{R}}(r=1) + (1-r^2) \bar{\mathcal{R}}(r=0) + \frac{r(r-1)}{2} \bar{\mathcal{R}}(r=-1). \quad (3.33)$$

In the present analysis we will consider only a standard WIMP–nucleus spin–dependent interaction with no explicit velocity dependence in the cross section. In this case only the integrated function  $\bar{\mathcal{R}}_0$  is needed to evaluate expected rates. For each experiment it can be tabulated as a function of  $E_R$  and for  $r = -1, 0, 1$ . Evaluations at run time for different values of  $m_\chi$ ,  $\delta$  and  $r$  can be obtained in a fast and efficient way through linear combinations of  $\bar{\mathcal{R}}_0$  interpolations using (3.31) and (3.33). Some examples of the functions  $\bar{\mathcal{R}}_0$  are plotted in Fig. 2 as a function of  $E_R$ .

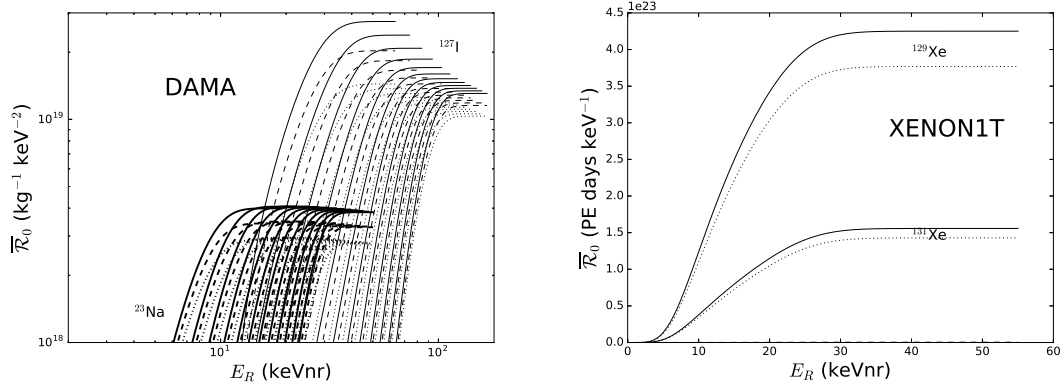


**Figure 2.** Left hand plot: integrated response functions  $\bar{\mathcal{R}}_0$  defined in Eqs.(3.30) and (3.32) as a function of  $E_R$  for the DAMA experiment [1]; right hand plot: the same for XENON1T[2]. As explained in Section 3 a different response function must be tabulated for each experimental energy bin, nuclear target (including different isotopes, see Eq.(3.15)) and for three values of the coupling ratio  $r = c^n/c^p$  (in order to perform the isospin rotation of Eq(3.33)). Including  $r = -1, 0, 1$ , all energetic bins and target isotopes with a non-vanishing spin-dependent response function this implies, for instance, 72 response functions for DAMA and 6 for XENON1T.

## 4 Results

In this Section we compare the pSIDM scenario reviewed in Section 2 to the current dark matter direct detection bounds listed in Appendix A in a statistical analysis where we wish to construct approximate 2D frequentist confidence intervals for the set of parameters  $\theta \equiv (m_\chi, \delta, r)$  with the velocity distribution treated as a set of nuisance parameters  $\eta$ . In order to do so, in the following we will consider both a halo-independent scenario and a more conventional Maxwellian velocity distribution. For a given dataset  $\mathbf{d}$ , including  $N_{DAMA}$  bins for the DAMA modulation amplitude and  $i = 1, \dots, N_{exp}$  experiments each with  $N_{bin}^i$  energy bins, we construct the Likelihood function:

$$-2 \ln \mathcal{L}(\mathbf{d}|\Theta) = \sum_{n=1}^{N_{DAMA}} \left( \frac{S_{1,n}(\Theta) - S_{1,n}^{exp}}{2\sigma_n^{exp}} \right)^2 - 2 \sum_{i=1}^{N_{exp}} \sum_{j=1}^{N_{bin}^i} \mathcal{L}_j^i(\Theta) \quad (4.1)$$

where  $\Theta = (\theta, \eta)$ , with

$$-2 \mathcal{L}_j^i(\Theta) = 2 \left[ S_{0,j}^i(\Theta) + B_j^i - N_j^i - N_j^i \ln \frac{S(\Theta)_{0,j}^i + B_j^i}{N_j^i} \right], \quad (4.2)$$

In Eq.(4.1)  $S_{1,n}$  is the prediction of the DAMA modulation amplitude in the  $n$ -th bin while  $S_{1,n}^{exp}$  the corresponding measurement with error  $\sigma_n^{exp}$ ,  $S_{0,j}^i$  the expected rate in the  $i$ -th energy bin of the  $j$ -th experiment with  $N_j^i$  the corresponding measured count rate and  $B_j^i$  the expected background. As far as the background is concerned, we notice that with the current level of required sensitivities its estimation is subject to large uncertainties. For this reason we assume the  $B_j^i$ 's as free parameters and minimize the likelihood with respect to them. This corresponds to taking:

$$-2\mathcal{L}_j^i(\Theta) = \begin{cases} 2 \left[ S_{0,j}^i(\Theta) - N_j^i - N_j^i \ln \frac{S(\Theta)_{0,j}^i}{N_j^i} \right] & \text{if } S_{0,j}^i(\Theta) > N_j^i \\ 0 & \text{otherwise.} \end{cases} \quad (4.3)$$

In the case of the PICASSO experiment[36] for each energy threshold  $E_i^{th}$  the number of observed events  $x_i^{exp}$  and 1-sigma Gaussian fluctuation  $\sigma_i$  normalized to events/kg/day is provided (see Table 2 in Appendix A). To include such constraint in our analysis we modify the likelihood function in the following way:

$$-2 \ln \mathcal{L}(\mathbf{d}|\Theta) \rightarrow -2 \ln \mathcal{L}(\mathbf{d}|\Theta) + \sum_i \left( \frac{x_i - x_i^{exp}}{\sigma_i} \right)^2 \Theta(x_i - x_i^{exp}) \quad (4.4)$$

with  $x_i$  the theoretical prediction of the corresponding detection rate.

We then construct approximate 2D and 1D frequentist confidence intervals for model parameters from an effective chi-square defined as  $\Delta\chi_{eff}^2 \equiv -2 \ln \mathcal{L}_{prof}/\mathcal{L}_{max}$  where  $\mathcal{L}_{max}$  is the maximum likelihood and:

$$\mathcal{L}_{prof}(\mathbf{d}, \theta_1) \propto \max_{\theta_2, \theta_3, \eta} \mathcal{L}(\mathbf{d}|\Theta) \text{ or } \mathcal{L}_{prof}(\mathbf{d}, \theta_1, \theta_2) \propto \max_{\theta_3, \eta} \mathcal{L}(\mathbf{d}|\Theta), \quad (4.5)$$

Wilks' theorem guarantees that under certain regularity conditions the corresponding distributions of  $\Delta\chi_{eff}^2$  converge to a chi-square distribution with 1 or 2 degrees of freedom [43].

The practical implementation of the method described above is conceptually quite simple but may require to explore a parameter space of large dimensionality (at least in the halo-independent approach). This kind of task is efficiently performed by using the technique of Markov chains, which makes use of the likelihood function itself to optimize the sampling procedure. To this aim we use the Markov-Chain Monte Carlo (MCMC) code emcee [20] to generate a large number of sets  $(\theta, \eta)$ .

#### 4.1 The halo-independent case

In the halo-independent approach we parameterize the halo function  $\tilde{\eta}_1$  with Eq.(3.24) subject to the conditions (3.22) and (3.27), and express  $\tilde{\eta}_0$  using (3.26), i.e. in terms of the *minimal* halo function that can explain the DAMA effect. In this way  $\Theta = (\theta, \eta) = (m_\chi, \delta, r, v_i, \delta\tilde{\eta}_1^i)$  with  $\theta = (m_\chi, \delta, r)$ ,  $\eta = (v_i, \delta\tilde{\eta}_1^i)$  and  $i = 1, \dots, N$ . As already pointed out, while in general the number of streams  $N$  would need to be arbitrarily large, in the pSIDM scenario moderate  $N$  values are expected to sample the halo functions well enough, since one has  $v_{min}^* < v_i < v_{esc}$  with  $v_{min}^* \rightarrow v_{esc}$ , so that the range of  $v_i$  is particularly compressed (for  $v_{esc}$  in this Section we assume  $v_{esc}=782$  km/s, which is obtained by combining a WIMP escape velocity  $u_{esc}=550$  km/s in the Galactic rest frame [44] with a rotational velocity of the Solar system  $v_0=220$  km/s [45] and a small peculiar velocity component, i.e.  $v_{esc} = u_{esc} + v_0 + 12$ ). Indeed, we have found that numerically the absolute maximum of the likelihood is achieved for  $N=4$  ( $-2 \ln \mathcal{L} \simeq 5.1$ ) and that the profile likelihood does not improve for larger values of  $N$ . In our results we combine  $N = 2, \dots, 8$  and for each value of  $N$  we generate a Markov chain of  $5 \times 10^6$  points using 250 independent walkers and a standard Metropolis-Hastings sampler, for a total of  $3.5 \times 10^7$  points. The outcome of this analysis is provided in Fig. 3, where the effective chi-square of Eq.(4.1) is plotted versus the three pSIDM parameters  $\theta_i = (m_\chi, \delta, r)$ . Their  $1\sigma$  confidence intervals can then be obtained through the condition:

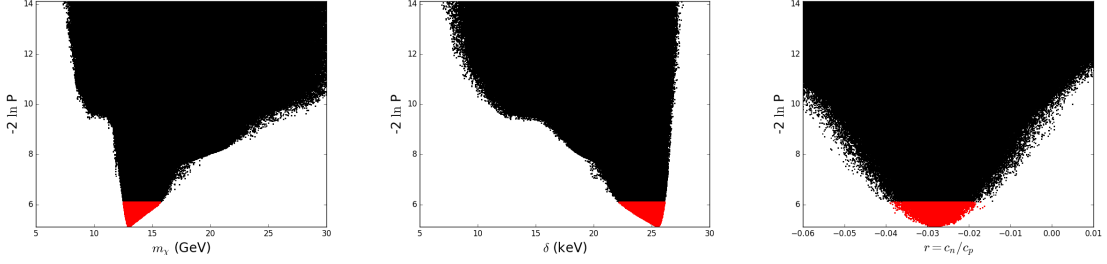


**Figure 3.** Profile likelihood of the WIMP mass  $m_\chi$  (left) the mass splitting  $\delta$  (center) and of the coupling ratio  $r$  (right) when the generalized halo functions  $\tilde{\eta}_{0,1}$  are parameterized in terms of Eqs.(3.24, 3.27, 3.26). Red points are subject to the condition (4.6.)

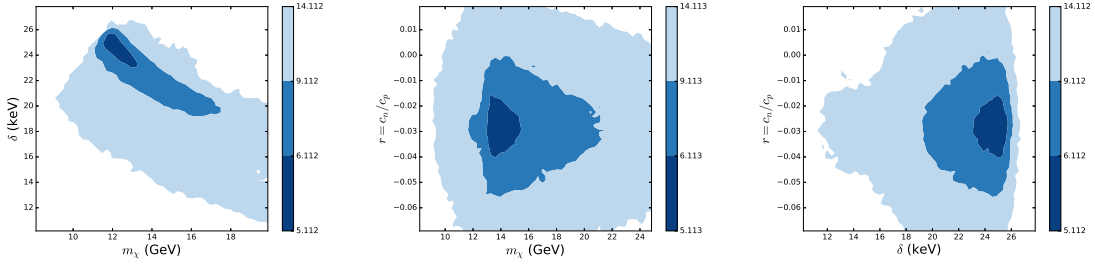


**Figure 4.** Correlations among the WIMP mass  $m_\chi$ , the mass splitting  $\delta$  and of the coupling ratio  $r$  plotted in Fig.(3). Dark shade:  $-2 \ln P < (-2 \ln P)_{min} + 1$ ; medium shade:  $-2 \ln P < (-2 \ln P)_{min} + 4$ ; light shade:  $-2 \ln P < (-2 \ln P)_{min} + 9$ .

$$\Delta(-2 \ln \mathcal{L}_{prof}(\theta_i)) \equiv -2 \ln \mathcal{L}_{prof}(\theta_i) + 2 \ln \mathcal{L}_{max} \leq 1, \quad (4.6)$$

with  $\mathcal{L}_{prof}(\theta_i)$  given by Eq.(4.5). In Fig. 3 the corresponding points are plotted in red. Notice that these  $1\sigma$  confidence intervals, sometime called  $1\sigma$  likelihood intervals, have a 68% coverage probability in the limit of large samples when the likelihood is well approximated by a Gaussian, but do not necessarily have a coverage probability of 68% if the likelihood is non-Gaussian, as is likely the case from inspection of Fig. 3. Correlations between couples of the parameters  $(m_\chi, \delta, r)$  can be obtained by plotting contour plots of  $\Delta(-2 \ln \mathcal{L}_{prof}(\theta_i))$ : the three corresponding plots are shown in Fig.(4), with  $1-\sigma$  likelihood intervals in dark blue.

Quantitatively, in the halo-independent case the  $1-\sigma$  likelyhood intervals for the pSIDM parameters turn out to be:

$$\begin{aligned} 12.5 \text{ GeV} &\leq m_\chi \leq 15.7 \text{ GeV} \\ 22.1 \text{ keV} &\leq \delta \leq 26.1 \text{ keV} \\ -0.039 &\leq r \leq -0.016. \end{aligned} \quad (4.7)$$

The fact that the value  $r=0$  is  $\simeq 2.4 \sigma$  away from the best-fit value signals tension with constraints from the neutron-odd targets  $^{129}\text{Xe}$  and  $^{131}\text{Xe}$  in XENON1T and PANDA. Indeed, the value  $r = c^n/c^p \simeq -0.03$  corresponds to a cancellation in the xenon spin-dependent

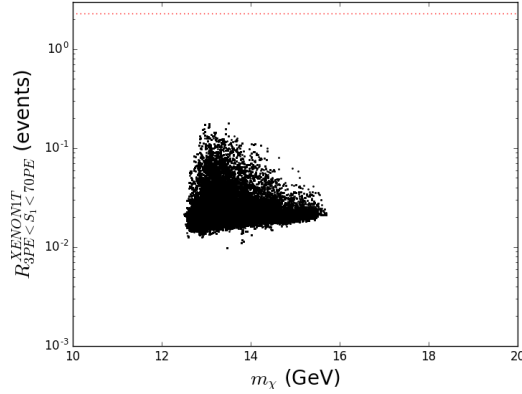


**Figure 5.** The expected rate in the upper half of the nuclear recoil band of the  $S_1$  (primary scintillation) full region of interest of XENON1T, corresponding to  $2 \text{ PE} < S_1 < 70 \text{ PE}$  (see Fig. 2 of Ref.[2]) is plotted vs. the WIMP mass  $m_\chi$  for the pSIDM configurations corresponding to the  $1-\sigma$  intervals of Eq.(4.7) and Figs. 3 and 4. The horizontal line represents the 90% C.L. upper bound for no nuclear-recoil candidates.

nuclear form factors for which, as already pointed out, we are using the determination from [8, 9]<sup>2</sup>. In light of this in Fig. 5 we show the expected rate in XENON1T in the upper half of the nuclear recoil band of the  $S_1$  (primary scintillation) full region of interest (corresponding to  $2 \text{ PE} < S_1 < 70 \text{ PE}$ , see Fig. 2 of Ref.[2]) as a function of the WIMP mass  $m_\chi$  for the pSIDM configurations corresponding to the  $1-\sigma$  intervals of Eq.(4.7) and Figs. 3 and 4. In the same plot the horizontal dashed line at 2.3 represents the 90% C.L. upper bound on the count rate corresponding to zero observed nuclear recoil candidates. From this plot one can see that with the current exposition ( $1.78 \times 10^4 \text{ kg day}$ ) the expected rate upper bound is approximately 0.2, i.e. one order of magnitude below the horizontal line. Since the first run of XENON1T was limited to only 34.2 live days[2], we conclude that one full year of data taking should allow XENON1T to reach the level of sensitivity required to start probing the pSIDM scenario.

## 4.2 The Maxwellian case

The most natural assumption for the thermalized component of the WIMP velocity distribution is a Maxwellian at rest in the Galactic rest frame with a cut-off corresponding to the escape velocity. In this case the halo functions  $\eta_{0,1}(v)$  are known, while to calculate the  $\tilde{\eta}_{0,1}(v)$ 's the cross-section  $\sigma_p$  is an additional free parameter. Expected rates can be calculated by directly performing the velocity integrals (3.17), an operation that is however time consuming when performed in a MCMC sampling. For this reason we keep using Eq.(3.31) to calculate expected rates, with the coefficients  $\tilde{\eta}_{0,1}^k$ , corresponding to averages of the halo functions  $\langle \eta_{0,1} \rangle_{[v_{k-1}, v_k]}$  in the velocity intervals  $v_{k-1} < v < v_k$ , calculated analytically. Specifically, indicating in the Galactic rest frame with  $v_{rms}$  the r.m.s. velocity of the Maxwellian,  $v_{Earth} = v_{Sun} + \Delta v_{Earth} \cos[\frac{2\pi}{T}(t - t_0)]$  the velocity of the Earth and with  $u_{esc}$  the escape velocity, they are given by:

<sup>2</sup>Two other determinations of the same form factors exist in the literature, Bonn-A and Nijmegen[46], for which the cancellation is at even lower values of  $r$ :  $r \simeq -0.05$  for the former and  $r \simeq -0.08$  for the latter.

$$\tilde{\eta}_{0,1}^k = \frac{\bar{\eta}_{0,1}(v_k) - \bar{\eta}_{0,1}(v_{k-1})}{v_k - v_{k-1}} \quad (4.8)$$

with:

$$\bar{\eta}_0(v) = \frac{N}{\eta\sqrt{\pi}} \begin{cases} \frac{\sqrt{\pi}}{2} [(x+\eta)\text{erf}(x+\eta) - (x-\eta)\text{erf}(x-\eta)] + \\ + \frac{1}{2} [e^{-(x+\eta)^2} - e^{-(x-\eta)^2}] - 2x\eta e^{-z^2}, & \text{if } x < z - \eta \\ \frac{\sqrt{\pi}}{2} [(x+\eta)\text{erf}(z) - (x-\eta)\text{erf}(x-\eta)] + \\ \frac{e^{-z^2}}{2} (\eta^2 - 2\eta x - 2\eta z + x^2 - 2xz + 1 + z^2) - \frac{1}{2} e^{(x-\eta)^2}, & \text{if } z - \eta < x < z + \eta \\ \sqrt{\pi}\eta\text{erf}(z) - 2\eta z e^{-z^2}, & x > z + \eta \end{cases} \quad (4.9)$$

and:

$$\bar{\eta}_1(v) = \frac{\Delta\eta}{\eta} (\delta\bar{\eta}_0(v) - \bar{\eta}_0(v)) \quad (4.10)$$

with:

$$\delta\bar{\eta}_0(v) = \frac{N}{\eta\sqrt{\pi}} \begin{cases} \frac{\sqrt{\pi}}{2} [\text{erf}(x+\eta) + \text{erf}(x-\eta)] - 2x\eta e^{-z^2}, & \text{if } x < z - \eta \\ \frac{\sqrt{\pi}}{2} [\text{erf}(z) + \text{erf}(x-\eta)] + (\eta - x - z)e^{-z^2}, & \text{if } z - \eta < x < z + \eta \\ \sqrt{\pi}\text{erf}(z) - 2ze^{-z^2}, & x > z + \eta \end{cases} \quad (4.11)$$

where  $x = \sqrt{3/2}v/v_{rms}$ ,  $\eta = \sqrt{3/2}v_{Sun}/v_{rms}$ ,  $\Delta\eta = \sqrt{3/2}\Delta v_{Earth}/v_{rms}$ ,  $z = \sqrt{3/2}u_{esc}/v_{rms}$  and  $N = [\text{erf}(z) - 2/\sqrt{\pi}ze^{-z^2}]^{-1}$ . In the isothermal sphere model hydrothermal equilibrium between the WIMP gas pressure and gravity is assumed, leading to  $v_{rms} = \sqrt{3/2}v_0$  with  $v_0$  the galactic rotational velocity, while  $v_{Sun} = v_0 + 12$ , accounting for a peculiar component. To evaluate Eq.(3.31) in our MCMC we have adopted  $N=50$ .

In the Maxwellian case an additional free parameter of the model is the WIMP–proton reference cross section  $\sigma_p$  introduced in Eq.(3.9), which represents a normalization factor for the experimental response functions. In particular we factorize  $\sigma_p$  by fixing the WIMP local density to the standard value  $\rho_\chi = 0.3 \text{ GeV/cm}^3$ . For the two parameters  $v_0$  and  $u_{esc}$  we take  $v_0 = (220 \pm 20) \text{ km/s}$  [45] and  $u_{esc} = (550 \pm 30) \text{ km/s}$  [44] assuming for both a Gaussian fluctuation in the likelihood, i.e. adding to latter the terms  $[(v_0 - 220)/20]^2 + [(u_{esc} - 550)/30]^2$ . As a consequence, we adopt the 6 parameters  $\Theta = (\theta, \eta)$ ,  $\theta = (\sigma_p, m_\chi, \delta, r)$ ,  $\eta = (v_0, u_{esc})$ . The results which correspond to such analysis are provided in Figs. 6, 7 and 8. Quantitatively, in this case the 1- $\sigma$  likelihood intervals for the pSIDM parameters turn out to be:

$$\begin{aligned} 3.54 \times 10^{-34} \text{ cm}^2 &\leq \sigma_p \leq 4.09 \times 10^{-33} \text{ cm}^2 \\ 11.4 \text{ GeV} &\leq m_\chi \leq 13.6 \text{ GeV} \\ 24.4 \text{ keV} &\leq \delta \leq 27.0 \text{ keV} \\ -0.035 &\leq r \leq -0.022. \end{aligned} \quad (4.12)$$

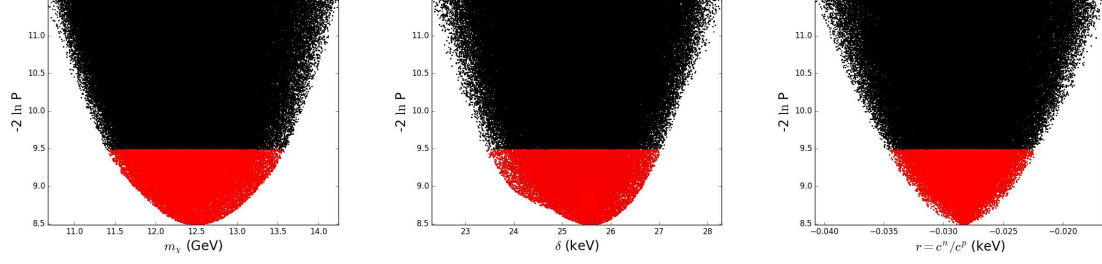


**Figure 6.** Profile likelihood of the WIMP mass  $m_\chi$  (left) the mass splitting  $\delta$  (center) and of the coupling ratio  $r$  (right) for a Maxwellian distribution with  $v_0=(220\pm 20)$  km/s and  $u_{esc}=(550\pm 30)$  km/s (assuming for both a corresponding Gaussian fluctuation in the likelihood). The color code is the same as in Fig.3.

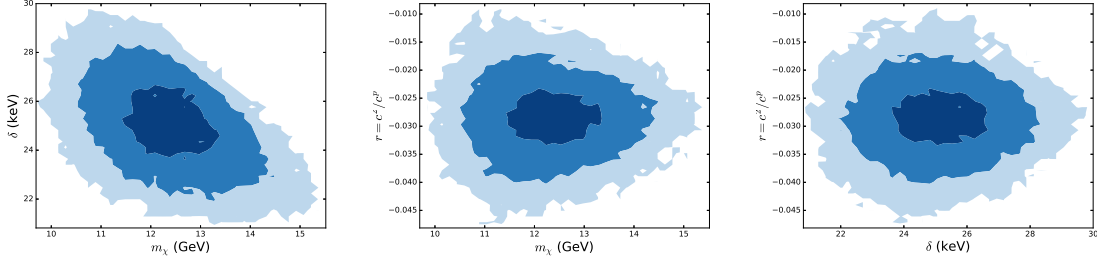


**Figure 7.** Correlations among the WIMP mass  $m_\chi$ , the mass splitting  $\delta$  and of the coupling ratio  $r$  for a Maxwellian distribution with  $v_0=(220\pm 20)$  km/s and  $u_{esc}=(550\pm 30)$  km/s (assuming for both a corresponding Gaussian fluctuation in the likelihood). The color codes is the same as in Fig.4.

## 5 Conclusions

In the present paper we have applied likelihood methods to the specific WIMP scenario of proton–philic spin–dependent inelastic Dark Matter (pSIDM), summarized in Section 2 and introduced in [19] to explain the DAMA yearly modulation effect [1] in compliance with the constraints from other direct detection DM searches. To this am, we obtained updated ranges for the model parameters  $m_\chi$  (WIMP mass),  $\delta$  (mass splitting) and  $r = c^n/c^p$  (neutron-to-proton coupling ratio) both in a halo–independent approach and adopting a truncated Maxwellian for the WIMP velocity distribution, constructing approximate frequentist confidence intervals from an effective chi–square including, among others, the latest experimental constraints from XENON1T [2], PANDAX-II [3], SuperCDMS [4] and CDMSlite [5]. In the halo–independent analysis we have implemented the dependence on the WIMP velocity distribution through the step–wise parameterization (3.24) of the halo-functions  $\tilde{\eta}_0$  and  $\tilde{\eta}_1$  defined in Eqs. (3.20) and (3.21) for the time–averaged and the time–modulated parts of the signal. In the pSIDM the WIMP incoming velocities required to explain the DAMA effect fall in a narrow range close to the escape velocity so that, in practice, a limited number of steps ( $N \leq 5$ ) in the the step–wise parameterization of the halo functions was sufficient to determine the profile likelihood of the parameters. Specifically, we have allowed the  $\tilde{\eta}_{1,k}$ ’s step values of the modulated halo function to vary freely, and parameterized the corresponding  $\tilde{\eta}_{0,k}$ ’s through



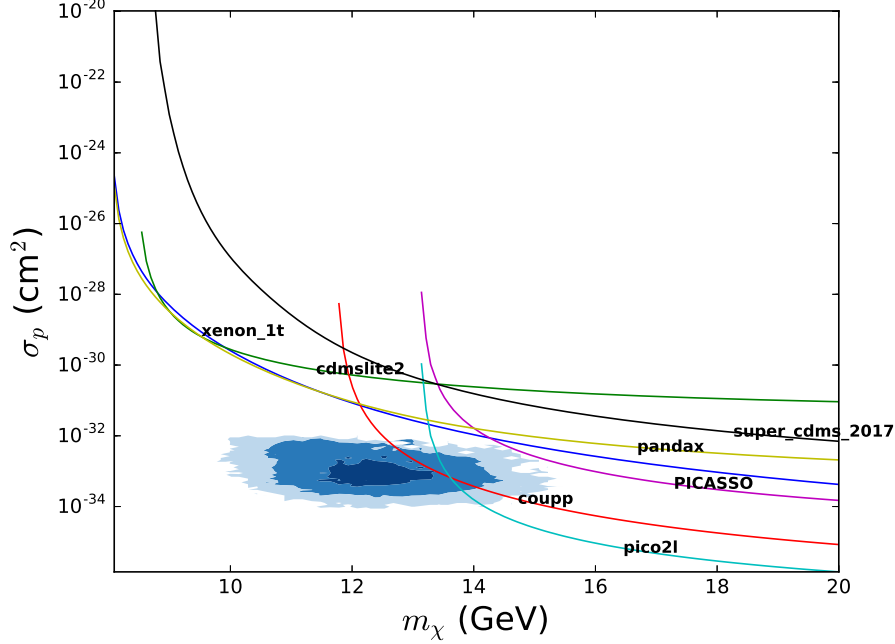


**Figure 8.** Two-dimensional profile of the WIMP mass  $m_\chi$  vs. the WIMP-proton conventional cross section  $\sigma_p$  defined in Eq.(3.9) for a Maxwellian distribution with  $v_0=(220\pm 20)$  km/s and  $u_{esc}=(550\pm 30)$  km/s (assuming for both a corresponding Gaussian fluctuation in the likelihood). The color code is the same as in Fig.3. Superimposed, a standard set of 90% C.L. exclusion plots where each experiment is analyzed independently. For all exclusion plots  $\delta=25.6$  keV and  $r=-0.028$ , which correspond to the absolute maximum of the likelihood function shown in Fig. 6.

Eqs.(3.27) and (3.26), i.e. in terms of the minimal time-averaged halo function compatible to a WIMP explanation of the DAMA effect. For the calculation of the profile likelihood of the pSIDM parameters we used emcee[20], a Markov Chain Montecarlo (MCMC) generator. The numerical procedure required a large number of evaluations of the expected rates, a time-consuming task when calculating the relevant experimental response functions at run time. For this reason in Section 3 we have introduced expected rates expressions rearranged in terms of differences of singled-valued integrated response functions suitable for a fast evaluation through tabulation and interpolation. Examples of such integrated response functions are provided in Fig.2.

Our frequentist analysis confirms the present viability of the pSIDM scenario as a possible explanation of the DAMA effect, with the 1-sigma parameter ranges of Eq.(4.7) for the halo-independent case, and of Eq.(4.12) when the WIMP velocity distribution is given by a standard truncated Maxwellian (the latter analysis also yields a range for the WIMP-proton cross section, as illustrated in Fig.8).

Although in the pSIDM scenario the response of neutron-odd targets is suppressed, our analysis signals some residual tension between DAMA and  $^{129}\text{Xe}$  and  $^{131}\text{Xe}$  in XENON1T and PANDA, since the best-fit value of the  $r = c^n/c^p$  parameter must be tuned to  $r = c^n/c^p \simeq -0.03$ , which corresponds to a cancellation in the xenon spin-dependent nuclear form factors. In particular, such value is  $\simeq 2.4 \sigma$  away from zero in the halo-independent

case and  $\simeq 4.8 \sigma$  away from zero for the Maxwellian case. As shown in Fig. 5, an order of magnitude improvement in the exposure of Ref.[2] (corresponding to a full year of data taking) should allow XENON1T to reach the level of sensitivity required to start probing the pSIDM scenario.

## Acknowledgments

This research was supported by the Basic Science Research Program through the National Research Foundation of Korea(NRF) funded by the Ministry of Education, grant number 2016R1D1A1A09917964.

## A Experimental constraints

In the present analysis we include the experimental data from DAMA[1],XENON1T[2], PANDAX-II[3], SuperCDMS[4], CDMSlite [5], PICO-2L[6], COUPP[7] and PICASSO[36].

### A.1 DAMA

We take the DAMA modulation amplitudes normalized to  $\text{kg}^{-1}\text{day}^{-1}\text{keVee}^{-1}$  from Ref.[1], assuming a constant quenching factor  $q=0.3$  for sodium and a Gaussian energy resolution  $\mathcal{G}(E', E_{ee}) = \text{Gauss}(E'|E_{ee}, \sigma) = 1/(\sqrt{2\pi}\sigma)\exp(-(E' - E_{ee})/2\sigma^2)$  with  $\sigma = 0.0091 (E_{ee}/\text{keVee}) + 0.448 \sqrt{E_{ee}}/\text{keVee}$  in keV.

### A.2 XENON1T and PANDAX-II

For xenon detectors the response functions given in Eq.(3.15) remain the same with the expected primary scintillation signal  $\langle S_1 \rangle$  in PE (photo-electrons) in place of the electron-equivalent energy  $E_{ee}$  and the quenching factor  $E_{ee}/E_R$  substituted by  $\langle S_1 \rangle / E_R = g_1 L_y$ , with  $g_1$  the light collection efficiency and  $L_y$  the light yield.

For XENON1T we have assumed zero WIMP candidate events in the range  $3 \text{ PE} \leq S_1 \leq 30 \text{ PE}$  in the lower half of the signal band, as shown in figure 2 of Ref.[2] for the primary scintillation signal  $S_1$  (directly in Photo Electrons, PE) for an exposure of 34.2 days and a fiducial volume of 1042 kg of Xenon. We have used the efficiency taken from Fig. 1 of [2], a light collection efficiency  $g_1=0.144$ , while for the light yield  $L_y$  we have used the NEST model of Ref. [47] with an electric field  $E=120 \text{ v/cm}$  and the parameters of Table 1 with the exception of the Lindhard parameter  $k=0.15$ , to reproduce the combined energy curves of Fig. 2b of [2].

On the other hand for PANDAX-II we included the result of Run 10 [3] with zero WIMP candidate events in the range  $3 \text{ PE} \leq S_1 \leq 45 \text{ PE}$  in the lower half of the signal band, as shown in figure 4, for an exposure of 77.1 days and a fiducial mass of 361.5 kg. From the supplemental material provided in [3] we have taken the efficiency in Fig.16 ,  $g_1=0.1114$  and  $L_y$  in Fig.13b.

For both XENON1T and PANDAX-II we have modeled the energy resolution combining a Poisson fluctuation of the observed primary signal  $S_1$  compared to  $\langle S_1 \rangle$  and a Gaussian response of the photomultiplier with  $\sigma_{PMT} = 0.5$ , so that:

$$\mathcal{G}_{Xe}(E_R, S) = \sum_{n=1}^{\infty} \text{Gauss}(S|n, \sqrt{n}\sigma_{PMT}) \text{Poiss}(n, \langle S(E_R) \rangle), \quad (\text{A.1})$$

with  $\text{Poiss}(n, \lambda) = \lambda^n / n! \exp(-\lambda)$ .

$E_{th}$ (keV)	exposure (kg day)	measured events
7.8	55.8	2
11	70	3
15.5	311.7	8

**Table 1.** For each operating threshold used in COUPP we provide the corresponding exposure and number of measured events used in our analysis.

$E_{th}$ (keV)	Event rate (events/kg/day)	Fluctuation
1.7	-6.0	7.1
2.9	-0.3	1.8
4.1	1.6	9.0
5.8	-0.2	9.2
6.9	0.0	1.3
16.3	1.4	1.7
39	0.2	1.7
55	1.3	4.7

**Table 2.** Observed number of events and 1-sigma statistical fluctuations (extracted from Fig. 5 of Ref.[36]) for each operating threshold used in PICASSO.

### A.3 PICO-2L, COUPP and PICASSO

Bubble chambers are threshold experiments, and in the response functions of Eq.(3.15) one has  $q(E_R)=1$  and:

$$\mathcal{G}_T(E', E_R) = \mathcal{P}_T(E_R)\delta(E' - E_R). \quad (\text{A.2})$$

For the nucleation probability of Fluorine we take:

$$\mathcal{P}_F(E_R) = 1 - \exp \left[ -\alpha_T \frac{E_R - E_{th}}{E_{th}} \right] \quad (\text{A.3})$$

with  $\alpha=5$ , while for Iodine we take  $\mathcal{P}_I=1$ .

PICO-2L uses  $C_3F_8$ . Its latest analysis [6] was performed after an upgrade of the detector that significantly reduced the background compared to [37]. Only the threshold  $E_{th}=3.3$  keV was analyzed, with a total exposure of 129.0 kg day and 1 event detected. We use for Fluorine and Carbon the nucleation probabilities of Fig. 4 of [37].

COUPP uses a  $CF_3I$  target. For each operating threshold used in COUPP the corresponding exposure and number of measured events are summarized in Table 1. For fluorine we use the nucleation probability of Eq.(A.3) with  $\alpha=0.15$ .

Finally, the PICASSO experiment[36] is a bubble chamber using  $C_3F_8$ , operated with eight energy thresholds. For each of the latter we provide the corresponding numbers of observed events and statistical fluctuations (normalized to events/kg/day and used in Eq.(4.4)) in Table 2 (extracted from Fig. 5 of Ref.[36]). We use the nucleation probability of Eq.(A.3) with  $\alpha_C=\alpha_F=5$ .

#### A.4 SuperCDMS and CDMSlite

CDMS operates thermal bolometers for which  $q=1$ . The latest SuperCDMS analysys [4] observes 1 event between 4 and 100 keVnr with an exposure of 1690 kg day. We take the efficiency from Fig.1 of [4] and  $\sigma = \sqrt{0.293^2 + 0.056^2 E_{ee}}$ .

For CDMSlite we consider the energy bin  $0.17 \text{ keV} < E' < 1.1 \text{ keV}$  with a measured count rate of  $1.1 \pm 0.2 \text{ [keV kg day]}^{-1}$  (Full Run 2 rate, Table II of Ref. [5]). We take the efficiency from Fig. 4 of [5] and  $\sigma = \sqrt{\sigma_E^2 + BE_R + (AE_R)^2}$ , with  $\sigma_E = 9.26 \text{ eV}$ ,  $A = 5.68 \times 10^{-3}$  and  $B = 0.64 \text{ eV}$  from Section IV.A.

#### References

- [1] R. Bernabei et al., *Final model independent result of DAMA/LIBRA-phase1*, *Eur. Phys. J. C* **73** (2013) 2648, [[arXiv:1308.5109](#)].
- [2] **XENON** Collaboration, E. Aprile et al., *First Dark Matter Search Results from the XENON1T Experiment*, *Phys. Rev. Lett.* **119** (2017), no. 18 181301, [[arXiv:1705.06655](#)].
- [3] **PandaX-II** Collaboration, X. Cui et al., *Dark Matter Results From 54-Ton-Day Exposure of PandaX-II Experiment*, *Phys. Rev. Lett.* **119** (2017), no. 18 181302, [[arXiv:1708.06917](#)].
- [4] **SuperCDMS** Collaboration, R. Agnese et al., *Results from the Super Cryogenic Dark Matter Search (SuperCDMS) experiment at Soudan*, [arXiv:1708.08869](#).
- [5] **SuperCDMS** Collaboration, R. Agnese et al., *Low-Mass Dark Matter Search with CDMSlite*, *Submitted to: Phys. Rev. D* (2017) [[arXiv:1707.01632](#)].
- [6] **PICO** Collaboration, C. Amole et al., *Improved dark matter search results from PICO-2L Run 2*, *Phys. Rev. D* **93** (2016), no. 6 061101, [[arXiv:1601.03729](#)].
- [7] **COUPP** Collaboration, E. Behnke et al., *First Dark Matter Search Results from a 4-kg CF<sub>3</sub>I Bubble Chamber Operated in a Deep Underground Site*, *Phys. Rev. D* **86** (2012), no. 5 052001, [[arXiv:1204.3094](#)]. [Erratum: *Phys. Rev. D* **90**, no. 7, 079902 (2014)].
- [8] A. L. Fitzpatrick, W. Haxton, E. Katz, N. Lubbers, and Y. Xu, *The Effective Field Theory of Dark Matter Direct Detection*, *JCAP* **1302** (2013) 004, [[arXiv:1203.3542](#)].
- [9] N. Anand, A. L. Fitzpatrick, and W. C. Haxton, *Weakly interacting massive particle-nucleus elastic scattering response*, *Phys. Rev. C* **89** (2014), no. 6 065501, [[arXiv:1308.6288](#)].
- [10] D. Tucker-Smith and N. Weiner, *Inelastic dark matter*, *Phys. Rev. D* **64** (2001) 043502, [[hep-ph/0101138](#)].
- [11] P. J. Fox, J. Liu, and N. Weiner, *Integrating Out Astrophysical Uncertainties*, *Phys. Rev. D* **83** (2011) 103514, [[arXiv:1011.1915](#)].
- [12] B. Feldstein and F. Kahlhoefer, *A new halo-independent approach to dark matter direct detection analysis*, *JCAP* **1408** (2014) 065, [[arXiv:1403.4606](#)].
- [13] P. J. Fox, Y. Kahn, and M. McCullough, *Taking Halo-Independent Dark Matter Methods Out of the Bin*, *JCAP* **1410** (2014), no. 10 076, [[arXiv:1403.6830](#)].
- [14] B. Feldstein and F. Kahlhoefer, *Quantifying (dis)agreement between direct detection experiments in a halo-independent way*, *JCAP* **1412** (2014), no. 12 052, [[arXiv:1409.5446](#)].
- [15] G. B. Gelmini, A. Georgescu, P. Gondolo, and J.-H. Huh, *Extended Maximum Likelihood Halo-independent Analysis of Dark Matter Direct Detection Data*, *JCAP* **1511** (2015), no. 11 038, [[arXiv:1507.03902](#)].

- [16] G. B. Gelmini, J.-H. Huh, and S. J. Witte, *Assessing Compatibility of Direct Detection Data: Halo-Independent Global Likelihood Analyses*, *JCAP* **1610** (2016), no. 10 029, [[arXiv:1607.02445](#)].
- [17] G. B. Gelmini, J.-H. Huh, and S. J. Witte, *Unified Halo-Independent Formalism Derived From Convex Hulls*, [arXiv:1707.07019](#).
- [18] P. Gondolo and S. Scopel, *Halo-independent determination of the unmodulated WIMP signal in DAMA: the isotropic case*, [arXiv:1703.08942](#).
- [19] S. Scopel and K.-H. Yoon, *Inelastic dark matter with spin-dependent couplings to protons and large modulation fractions in DAMA*, *JCAP* **1602** (2016), no. 02 050, [[arXiv:1512.00593](#)].
- [20] D. Foreman-Mackey, D. W. Hogg, D. Lang, and J. Goodman, *emcee: The MCMC Hammer*, *Publ. Astron. Soc. Pac.* **125** (2013) 306–312, [[arXiv:1202.3665](#)].
- [21] **LUX** Collaboration, D. S. Akerib et al., *First results from the LUX dark matter experiment at the Sanford Underground Research Facility*, *Phys. Rev. Lett.* **112** (2014) 091303, [[arXiv:1310.8214](#)].
- [22] **LUX** Collaboration, D. S. Akerib et al., *Improved Limits on Scattering of Weakly Interacting Massive Particles from Reanalysis of 2013 LUX Data*, *Phys. Rev. Lett.* **116** (2016), no. 16 161301, [[arXiv:1512.03506](#)].
- [23] D. S. Akerib et al., *Results from a search for dark matter in the complete LUX exposure*, [arXiv:1608.07648](#).
- [24] **PandaX** Collaboration, A. Tan et al., *Dark Matter Search Results from the Commissioning Run of PandaX-II*, *Phys. Rev.* **D93** (2016), no. 12 122009, [[arXiv:1602.06563](#)].
- [25] **PandaX-II** Collaboration, A. Tan et al., *Dark Matter Results from First 98.7 Days of Data from the PandaX-II Experiment*, *Phys. Rev. Lett.* **117** (2016), no. 12 121303, [[arXiv:1607.07400](#)].
- [26] **CDMS-II** Collaboration, Z. Ahmed et al., *Results from a Low-Energy Analysis of the CDMS II Germanium Data*, *Phys. Rev. Lett.* **106** (2011) 131302, [[arXiv:1011.2482](#)].
- [27] **SuperCDMS** Collaboration, R. Agnese et al., *Search for Low-Mass Weakly Interacting Massive Particles Using Voltage-Assisted Calorimetric Ionization Detection in the SuperCDMS Experiment*, *Phys. Rev. Lett.* **112** (2014), no. 4 041302, [[arXiv:1309.3259](#)].
- [28] **SuperCDMS** Collaboration, R. Agnese et al., *Search for Low-Mass Weakly Interacting Massive Particles with SuperCDMS*, *Phys. Rev. Lett.* **112** (2014), no. 24 241302, [[arXiv:1402.7137](#)].
- [29] **SuperCDMS** Collaboration, R. Agnese et al., *Improved WIMP-search reach of the CDMS II germanium data*, *Phys. Rev.* **D92** (2015), no. 7 072003, [[arXiv:1504.05871](#)].
- [30] S. C. Kim et al., *New Limits on Interactions between Weakly Interacting Massive Particles and Nucleons Obtained with CsI(Tl) Crystal Detectors*, *Phys. Rev. Lett.* **108** (2012) 181301, [[arXiv:1204.2646](#)].
- [31] Y. Kim, *Recent progress in KIMS experiment*, talk given at 13<sup>th</sup> International Conference on Topics in Astroparticle and Underground Physics, September 8–13 2013, Asilomar, California USA (TAUP2013).
- [32] H. S. Lee et al., *Search for Low-Mass Dark Matter with CsI(Tl) Crystal Detectors*, *Phys. Rev.* **D90** (2014), no. 5 052006, [[arXiv:1404.3443](#)].
- [33] P. Ullio, M. Kamionkowski, and P. Vogel, *Spin dependent WIMPs in DAMA?*, *JHEP* **07** (2001) 044, [[hep-ph/0010036](#)].

- [34] E. Del Nobile, G. B. Gelmini, A. Georgescu, and J.-H. Huh, *Reevaluation of spin-dependent WIMP-proton interactions as an explanation of the DAMA data*, *JCAP* **1508** (2015), no. 08 046, [[arXiv:1502.07682](#)].
- [35] M. Felizardo et al., *Final Analysis and Results of the Phase II SIMPLE Dark Matter Search*, *Phys. Rev. Lett.* **108** (2012) 201302, [[arXiv:1106.3014](#)].
- [36] **PICASSO** Collaboration, S. Archambault et al., *Constraints on Low-Mass WIMP Interactions on  $^{19}\text{F}$  from PICASSO*, *Phys. Lett.* **B711** (2012) 153–161, [[arXiv:1202.1240](#)].
- [37] **PICO** Collaboration, C. Amole et al., *Dark Matter Search Results from the PICO-2L  $\text{C}_3\text{F}_8$  Bubble Chamber*, *Phys. Rev. Lett.* **114** (2015), no. 23 231302, [[arXiv:1503.00008](#)].
- [38] **PICO** Collaboration, C. Amole et al., *Dark Matter Search Results from the PICO-60  $\text{CF}_3\text{I}$  Bubble Chamber*, *Submitted to: Phys. Rev. D* (2015) [[arXiv:1510.07754](#)].
- [39] S. Scopel, K.-H. Yoon, and J.-H. Yoon, *Generalized spin-dependent WIMP-nucleus interactions and the DAMA modulation effect*, *JCAP* **1507** (2015), no. 07 041, [[arXiv:1505.01926](#)].
- [40] E. Del Nobile, G. Gelmini, P. Gondolo, and J.-H. Huh, *Generalized Halo Independent Comparison of Direct Dark Matter Detection Data*, *JCAP* **1310** (2013) 048, [[arXiv:1306.5273](#)].
- [41] P. Gondolo and S. Scopel, *Halo-independent determination of the unmodulated WIMP signal in DAMA: the isotropic case*, *JCAP* **1709** (2017), no. 09 032, [[arXiv:1703.08942](#)].
- [42] A. Ibarra and A. Rappelt, *Optimized velocity distributions for direct dark matter detection*, *JCAP* **1708** (2017), no. 08 039, [[arXiv:1703.09168](#)].
- [43] F. Feroz, K. Cranmer, M. Hobson, R. Ruiz de Austri, and R. Trotta, *Challenges of Profile Likelihood Evaluation in Multi-Dimensional SUSY Scans*, *JHEP* **06** (2011) 042, [[arXiv:1101.3296](#)].
- [44] T. Piffl et al., *The RAVE survey: the Galactic escape speed and the mass of the Milky Way*, *Astron. Astrophys.* **562** (2014) A91, [[arXiv:1309.4293](#)].
- [45] S. E. Koposov, H.-W. Rix, and D. W. Hogg, *Constraining the milky way potential with a six-dimensional phase-space map of the  $gd-1$  stellar stream*, *The Astrophysical Journal* **712** (2010), no. 1 260.
- [46] M. T. Ressell and D. J. Dean, *Spin dependent neutralino - nucleus scattering for  $A$  approximately 127 nuclei*, *Phys. Rev.* **C56** (1997) 535–546, [[hep-ph/9702290](#)].
- [47] B. Lenardo, K. Kazkaz, A. Manalaysay, J. Mock, M. Szydagis, and M. Tripathi, *A Global Analysis of Light and Charge Yields in Liquid Xenon*, *IEEE Trans. Nucl. Sci.* **62** (2015), no. 6 3387–3396, [[arXiv:1412.4417](#)].